Development of an Active Grid Adapted to a Low-Swirl Burner and Measurements of Turbulent Properties of the Flow Field

Inkyu Jeon, Shigeru Tachibana, Laurent Zimmer, Akira Nishizawa

ISSN 1349-1113
JAXA-RR-05-055E

JAXA Research and Development Report

Development of an Active Grid Adapted to a Low-Swirl Burner and Measurements of Turbulent Properties of the Flow Field

Inkyu JEON, Shigeru TACHIBANA, Laurent ZIMMER
and Akira NISHIZAWA

March 2006

Japan Aerospace Exploration Agency

JAXA-RR-05-055E

JAXA Research and Development Report
宇宙航空研究開発機構研究開発報告

Development of an Active Grid Adapted to a Low-Swirl Burner and Measurements of Turbulent Properties of the Flow Field

弱旋回バーナーに適合したアクティブグリッドの開発と流れ場の乱流特性の計測

Inkyu JEON*1, Shigeru TACHIBANA*1, Laurent ZIMMER*1 and Akira NISHIZAWA*2

全　仁圭*1、立花　繁*1、ジマー・ロレント*1、西沢　啓*2

＊1　Aeroengine Technology Center, Institute of Aerospace Technology
総合技術研究本部　航空エンジン技術開発センター
＊2　Aerodynamics Research Group, Institute of Aerospace Technology
総合技術研究本部　空気力学研究グループ

March 2006
2006 年 3 月

Japan Aerospace Exploration Agency
宇宙航空研究開発機構

Development of an Active Grid Adapted to a Low-Swirl Burner and Measurements of Turbulent Properties of the Flow Field

Inkyu Jeon[1], Shigeru Tachibana[1], Laurent Zimmer[1] and Akira Nishizawa[2]

[1]Aeroengine Technology Center, Institute of Aerospace Technology

[2]Aerodynamics Research Group, Institute of Aerospace Technology

Abstract

The aim of this research is to design a bi-plane active grid to enhance turbulent flow downstream of a low-swirl burner. The active grid is a variation of the original form devised by Makita in 1991. First, adequate ranges for experimental parameters are sought using non-reacting flow. While turbulent intensity is of major interest, homogeneity, isotropy, and integral scale near the nozzle exit are also analyzed by measuring mean and turbulent velocities. In addition, a fully developed inertial subrange is demonstrated by energy spectra analysis. When premixed reacting flow is tested, a turbulent Karlovitz number higher than unity is achieved under various conditions. It indicates that the flame produced is in the thin reaction zone regime on the Peters' diagram. The measurements are implemented using both hot-wire anemometry and particle image velocimetry.

Nomenclature

c	Reynolds mean progress variable
E_{vv}	Power spectrum density in streamwise direction [m²/s]
f	Frequency [s⁻¹]
Ka	Turbulent Karlovitz number [-]
L_1	Pipe length after swirler [mm]
L_2	Pipe length between swirler and active grid [mm]
l	Integral length [mm]
l_F	Laminar flame thickness [mm]
M	Active grid mesh size [mm]
p_{AG}	Switching period [pulse, 1 pulse = 0.36 degree]
Q_m	Flow rate of main mixture [NLM, Normal Liter per Minute]
Q_{air}	Flow rate of main air [NLM]
Q_{swl}	Flow rate of secondary air through swirl generator [NLM]
S	Swirl number [-]
s_L	Laminar flame propagating velocity [m/s]
V	Mean velocity in streamwise direction [m/s]
v'	Turbulent velocity in streamwise direction [m/s]
y	Streamwise coordinate [mm]
ε	Energy dissipation rate [m²/s³]
κ	Wave number [m⁻¹]
υ	Dynamic viscosity [m²/s]
ω_{AG}	Rotating speed of active grid axis [rps, Revolutions Per Second]

1. Introduction

As regulation on NOx emissions from gas-turbines has become stricter, lean-premixed combustion has more importance nowadays. In one of the various attempts to investigate such flame, Cheng (1995) developed a low-swirl burner (LSB) to inject small tangential secondary flow into main flow. Cheng and Fable (2001) pointed that the LSB has several remarkable aspects; (1) low NOx-emission, (2) no recirculation zone, though it is not the case for all conditions, (3) free of large velocity gradient in axial and radial directions, (4) stable flame even with intense turbulence. Also, (5) it has a simple mechanical structure, and (6) is suitable for laser optical measurement of flame. Bedat and Cheng (1995) were successful to generate quite strong turbulent flame by applying a slot style turbulence generator, originally developed by Videto and Santavicca (1991), to the LSB. In their work, the turbulent flame enters the thin reaction zones regime (Fig. 1) which has been considered as a common regime in practical combustion systems, but difficult to observe in laboratory environments.

In JAXA, several works on the lifted premixed flame sustained by a LSB similar to the Cheng's original burner have been conducted (Tachibana et al., 2004, Zimmer et al., 2004). Their burner used a perforated plate as a turbulence generator and the flames

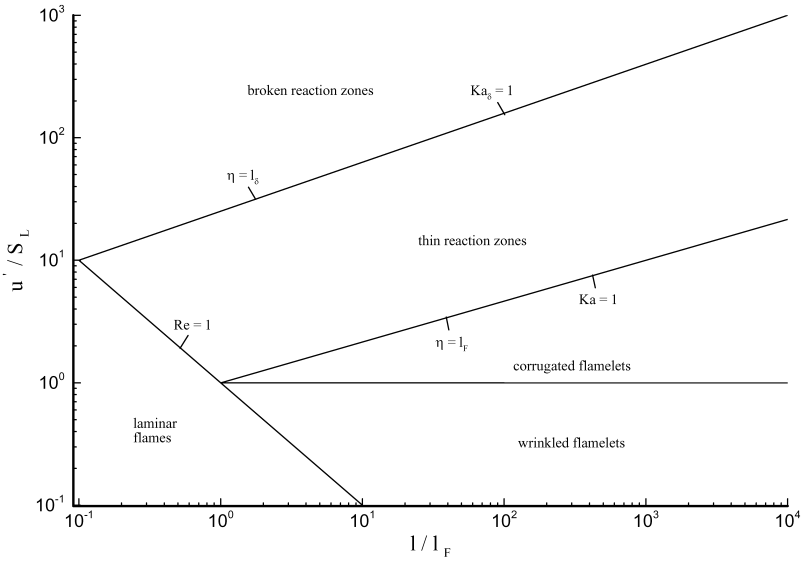

Fig. 1 Regime diagram for turbulent premixed combustion, Peters (2000)

were reported to appear in the regime of corrugated flamelets. For instance, Tachibana et al. (2004) generated a turbulent flame of l=9 mm, v'=0.534 m/s on the condition of ϕ =0.72, s_L=0.207 m/s, and l_F=0.298 mm, which means turbulent Karlovitz number, Ka, is 0.753. In order to study turbulent flame in the thin reaction zones regime using the same burner, stronger turbulent intensity is required.

Makita (1991) showed that a bi-plane active grid with randomly rotating flapping wings can induce much stronger turbulent flow than passive grids do. Apart from high turbulent intensity, Makita succeeded in generating fully-developed, quasi-isotropic, and homogeneous turbulent flow in a wind tunnel using the active grid. Since then, several researchers like Mydlarski and Warhaft (1996), Poorte and Biesheuvel (2002), Kang et al. (2003), and Larssen and Devenport (2003) have favored active grids based on the Makita's design to investigate properties of strong turbulent flow. While this type of active grid is suitable for generating higher turbulent intensity, it also has been reported to produce larger integral scale than previous results. It makes the inertial subrange of the energy spectra wider. A -5/3 slope sustains over two orders of magnitude in wave number. From the point of view of the regime diagram, this tendency of large integral scale makes the thin reaction zones flame difficult to achieve because larger integral scale requires stronger turbulence intensity to get into the thin reaction zones regime (see figure 1). No research has been conducted to use the Makita-style active grid to study turbulent reacting flow. In this research, we aim to generate turbulent flow strong enough to achieve the thin reaction zones flame by implementing the Makita-style active grid to the present LSB system, keeping integral scale as small as possible. First, the influence of various active grid operation modes on turbulent flow properties is studied. Then, effective flow conditions are provided. Once these tests are done with cold flow, selected experimental parameters are used for reacting flow to find out flame regime information.

2. Development of an active grid adapted to the LSB

The developed active grid follows the design of Makita (1991). Generally, other active grids contain about 10 by 10 rods to make a core area as broad as possible. However, the grid in this work consists of only three horizontal and three vertical rods due to a small scale of the system, as shown in Fig. 2.

The inner diameter of a nozzle is 53.0 mm, and a mesh size, M, is 13.25 mm. The diameter of the 9 rods is decided to be 4 mm to adapt a criterion for blockage ratio proposed by Mehta and Hoffmann (1987). Because the LSB uses a circular nozzle, the grid also has to be adapted to circular cross-section. As a result, all wings do not have an identical shape. In the central part, 24 wings of the same shape are positioned to guarantee a core as large area as pos-

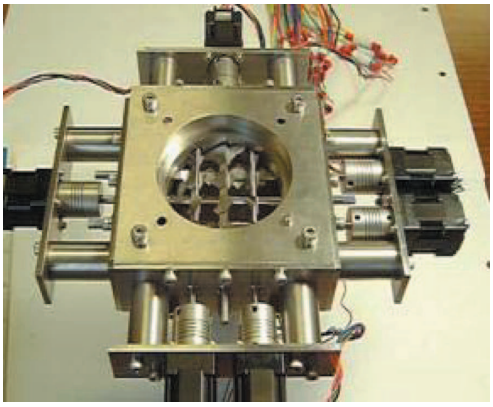

Fig. 2 The active grid after assembly was completed

sible. The remaining area is fully covered with exactly fit wings rather than the central type (Fig. 3, left). It is because, if the area near boundary is unblocked, resulting flow will likely become non-uniform. Detailed designs for whole components of the active grid are presented in Appendix A.

All parts including six rods of 4 mm in diameter and wings of 0.5 mm in thickness are made of stainless steel. As shown in Fig. 3(middle), wings are fixed on 1 mm deep cuts on a circular rod by using 2 metal pins for each wing. The scale and the material do not allow the attachment work to be carried out in the small space of the duct of diameter 53 mm easily. Hence, the body of the active grid is designed as three parts like Fig. 3(right) so that an assembly of wing-rod can be set up without difficulty. Each rod is connected to an electric motor through one coupling, and supported by two bearings at both ends of the body. The bearings do not only function as mechanical supporters, but also provide sealing for the flow inside. Table 1 shows the list of the components used for the driving motor system, and Fig. 4 describes connections between them.

Rods can rotate independently to each other, controlled by a LabVIEW programme installed on a laptop PC. The basic structure of this programme is provided by the motor producer, SIGMA KOKI (http://www.sigma-koki.com/), and is modified for multiple motor usage and easier control of necessary operation parameters. Rotating speed, direction, and direction switching period can be decided randomly each period, for an example of a typical condition, in the range of 1-2.5 revolutions per second (rps), clockwise or anticlockwise, and 0.165-1.000 seconds (or 200-1000 pulses in rotating angle, here 1 pulse means 0.36 degrees), respectively. Rotating speeds faster than 2.5 rps are unavailable because some of the rods show intermittent stops during operation under those

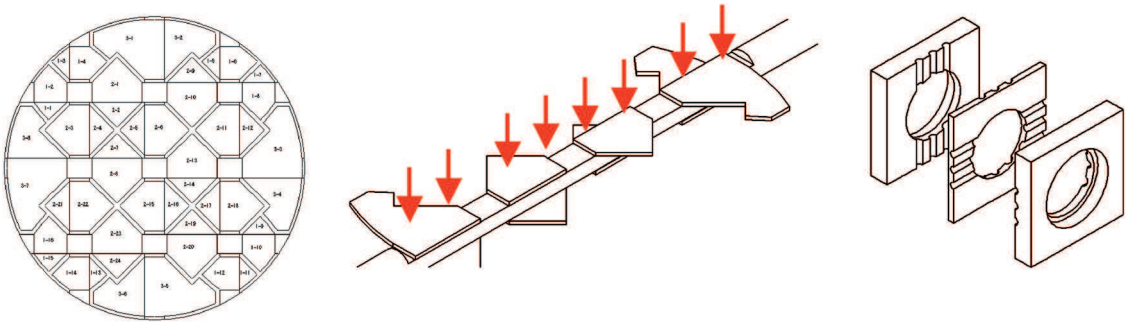

Fig. 3 (left) Array of wings (middle) Central rod and wings attached on it. Eight red arrows show positions of stainless steel pins of ϕ=1.5 mm (right) Three parts of the body of the active grid

Table 1 Motor-related components

	Model	Number
Motor	Tamagawa seiki, TS3682N4 stepping motor	6
Bearing	NSK, MR84ZZ	12
Coupling	Miki pulley, Heli-cal coupling 1441	6
Motor driver	SIGMA KOKI, CSG 602R	3
I/F converter	SIGMA KOKI, IFI-22R	1

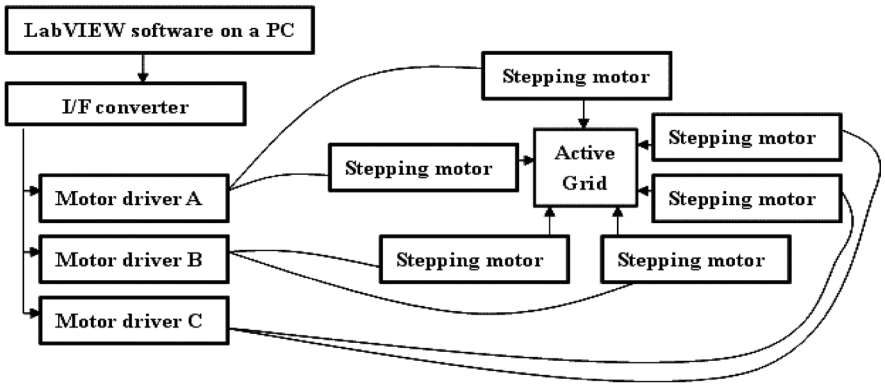

Fig. 4 Schematic of the motor controlling system

conditions. It is considered to be due to the hardware limit of the CSG 602R drivers. Switching periods shorter than 0.165 seconds are also not available with the present system because one loop for a set of six commands in the computer program takes 0.165 seconds to be carried out. However, it does not seem to be a problem of CPU of a particular PC. When it is not connected to the active grid, the PC used in the experiments is capable of calculating much faster. So, it must result from communication between the PC and the converter / drivers or internal mechanism of a converter / drivers. For comparison, various constant modes where a rotating speed or a period is fixed for all rods have also been tested. The result is described in section 4.1.

Fig.5 show the structure of the LSB composed of a circular nozzle, a swirl generator and an active grid. The active grid locates upstream of the swirl generator, and the distance between them is 100-450 mm (200 mm as a default). While many researchers have measured flow properties at the distance up to $80M$~$100M$, our facility has space limitation in the streamwise direction because of a ventilating duct and a flow supply system. As a result, up to about $35M$ may be available for measurements. The swirl generator has four small orifices to inject secondary air in tangential direction. The geometric swirl number S is defined as the ratio between the axial flux of angular momentum divided by the axial flux of axial momentum times the nozzle radius. It is expressed by the following equation in the jet-type LSB (Johnson and Cheng (2003)).

$$S = \frac{\pi R^2 Q_{swl}^2 \cos\alpha}{n\pi R_{swl}^2 (Q_m + Q_{swl})^2}$$

Here, n means the number of injection orifices in the swirl generator, R_{swl} the diameter of injection holes, R the diameter of the main passage, α the relative angle. In this case, actual values of n, R_{swl}, R and α are 4, 1 mm, 26.5 mm and 20 deg, respectively.

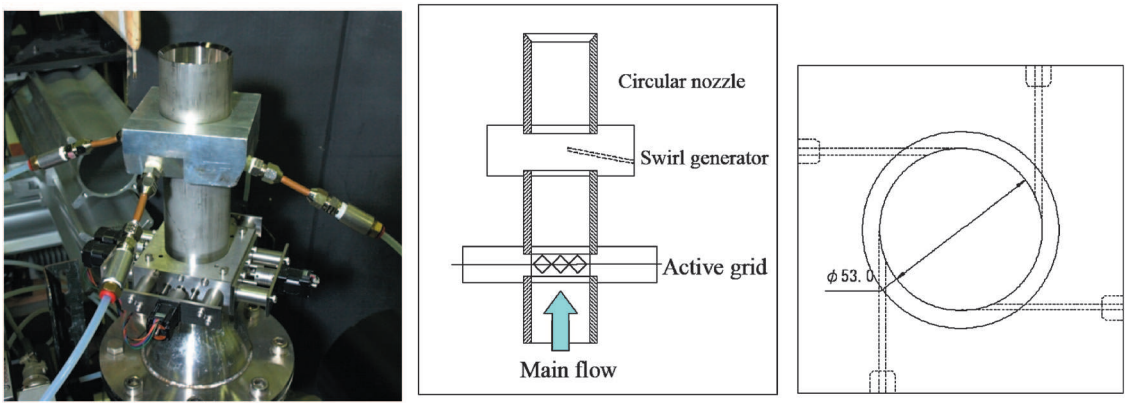

Fig. 5 Structure of the low-swirl burner; (left) picture of the burner, (middle) schematic of the burner, (right) schematic of the cross section of the swirl generator.

3. Measurement methods

3.1 Hot-wire anemometer

A constant temperature hot-wire anemometer used in this experiment is of a one-dimensional, uni-directional type, or, namely, I-probe. The hot-wire probe is made of a tungsten filament with copper coating, 5 μm in diameter and 2 mm in length. Before every experiment, the hot-wire anemometer is calibrated using a pressure transducer and a Pitot tube in uniform flow of known flow rate. Assuming that velocity information from the Pitot tube is correct, the following King's Law (King, 1914) provides a conversion equation between hot-wire voltage and velocity;

$$E^2 = A + B * V^{0.45}$$

, where A and B are constant coefficients, E is the voltage from the hot wire, and V is the velocity from the Pitot tube when proceeding with the calibration. Measured voltage is recorded using a 24 bits A/D converter board, PXI-4472 of National Instrument Corporation, with the software named CAT-SYSTEM of CATEC Incorporated. All post-processing work is carried out by in-house MATLAB codes. All interesting properties except low frequency peaks may be understood with high frequency sampling. Hence, for one condition set, there need two measurements using high and low sampling frequencies. Low frequency data is measured with sampling rate of 256 Hz during 128 seconds, and high frequency one with 25.6 kHz during 20.48 seconds.

3.2 Particle Image Velocimetry (PIV) system

The measurement system for the PIV is composed of a Gemini-PIV Nd:YAG laser of New Wave Research (15Hz at 120mJ/pulse) and a PowerView 4M CCD camera of TSI (2048*2048 pixels with a dynamic range of 12 bits). An interferential filter centered on 532nm is used to remove natural emission of flame and therefore to improve signal to noise ratio. These devices are synchronized by a synchroniser Model-610034 of TSI incorporate. As for tracer particles, DEHS liquid is atomized to droplets of order of 1 μm in a mean diameter by the Six-jet atomizer Model-9306 of TSI incorporated, then injected into the main flow. The field of view is for the most cases a rectangular area of 129.6 mm by 112.8 mm, but some view of bottom area is hindered by the nozzle exit. Another size of 56.9 mm by 53.3 mm is also used for reacting flow measurement. For each condition, 500 couples of images are taken.

4. Results and discussion

4.1 Influence of active grid operating mode on low-frequency oscillations

To see the effects of operating modes of the active grid, hot-wire measurements are carried out on various combinations of w_{AG} and, p_{AG} under the following conditions; $Q_m = Q_{air}$=662NLM, S=1.14, L_1=90mm, L_2=200mm. For a fixed rotating speed, a series of peaks are seen at low frequency range of energy spectra plots (Fig. 6). Poorte and Biesheuvel (2002) already pointed that these peaks would appear at mul-

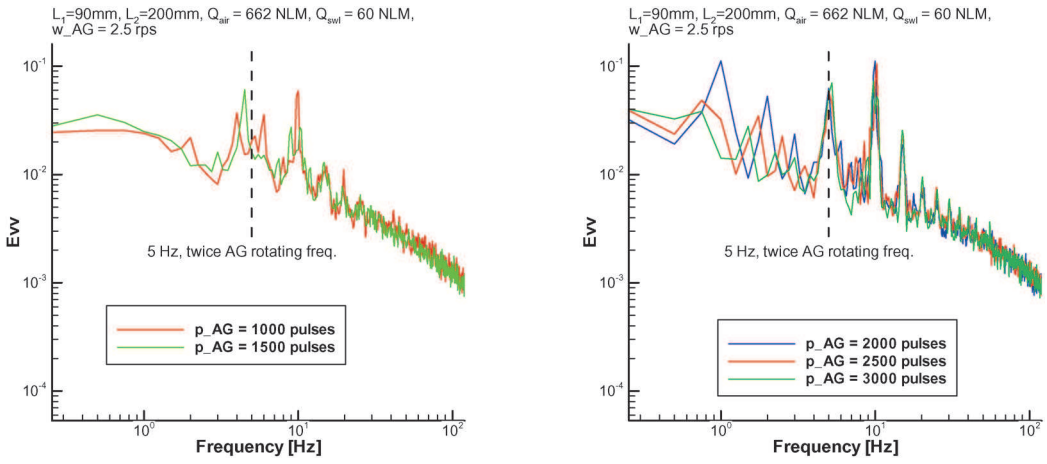

Fig. 6 Relation between p_{AG} and low-frequency peaks; (left) shorter periods (p_{AG}=1000 and 1500), (right) longer periods (p_{AG}=2000, 2500, 3000). The data are taken at the location, y=10mm on the center line.

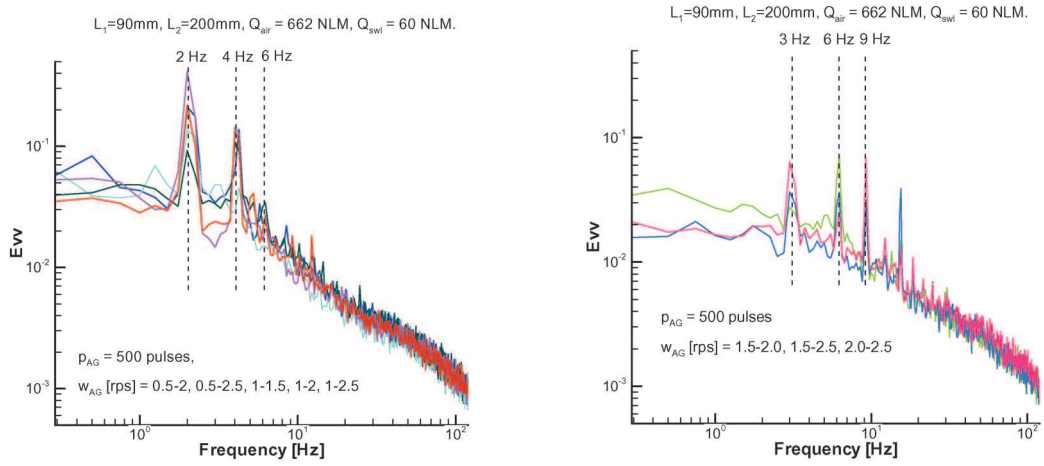

Fig. 7 Effect of random rotating speed under constant short period condition. (left) ω_{AG} =0.5-2.0, 0.5-2.5, 1.0-2.5, 1.0-1.5, 1.0-2.0, 1.0-2.5; (right) ω_{AG} =1.5-2.0, 1.5-2.5, 2.0-2.5. The data are taken at the location, y=10mm on the center line.

tiples of twice the rotating frequency. In Fig. 6, rotating speed is fixed at 2.5 rps, and the first peak is located at 5 Hz. But, there is slight dependency on switching period. With shorter periods, positions are not exactly multiples of 5 Hz. On the other hand, with longer ones, peaks appear at exactly 5 Hz, 10 Hz, 15 Hz, and so on. Also, another series of peaks exists only with the latter case. These distinct low frequency peaks may result in flame oscillation or instability when reacting flow is used. Hence, it is desirable to remove them for it is aimed to apply the same conditions to reacting flow.

With random speed option on, peak positions are multiples of 2 Hz or 3 Hz (Fig. 7). Not only for the conditions shown here, but for other random speed settings is found one of these two trends. Nevertheless, combinations of random rotating speed and constant short period conditions tend to give smaller low frequency peaks (see Fig. 7). When both rotating speed and period are decided randomly, low frequency peaks almost disappear (Fig. 8). Therefore, it is helpful to use this double random mode so as to avoid low frequency oscillations. Also, for comparison, a 'passive' mode is used, where all wings are fixed in the streamwise direction so that only rod frames face incoming air flow and the maximum flow area is allowed.

4.2 Mean and root-mean-square (rms) velocity

To measure flow properties on the double random mode, hot-wire and PIV measurements are carried

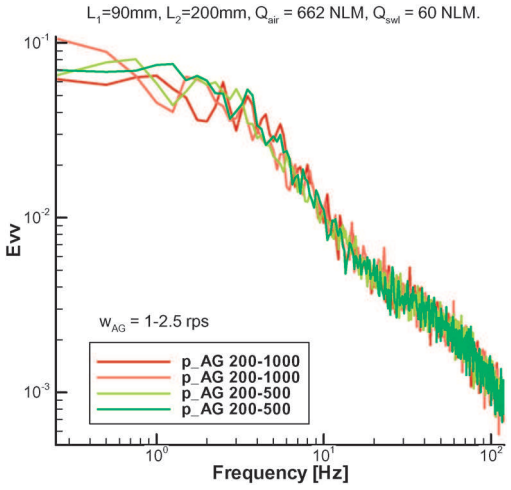

Fig. 8 Results with random rotating speed and random switching period. The data are taken at the location, y=10mm on the center line.

out on an operating mode, w_{AG}=1.0-2.5rps and p_{AG}=200-1000 pulses, under the following conditions; Q_m=Q_{air}=662NLM, S=1.14, L_1=90mm, L_2=200mm.

As shown in Fig. 9, velocities are strongly influenced by the swirl number. As the swirl number becomes larger, mean velocity decreases and rms velocity increases as measured by hot-wire anemometer and PIV. The PIV mean velocity is not much different from the hot-wire result for the whole range of the swirl number while turbulent fluctuation deviates increasingly at only the large swirl number range. As a result, relative turbulent intensity from the PIV measurements is also almost identical to one by hot-wire anemometer for a wide range of swirl number, both reaching about 50% at S=2.00. Velocity

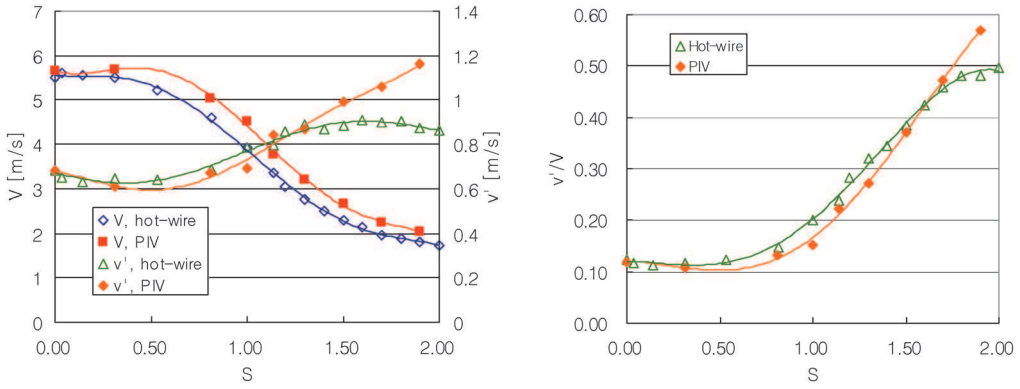

Fig. 9 Effect of swirl number (left) on mean and turbulent velocities, and (right) on relative turbulent intensity at y=10mm on the centerline.

properties change most drastically between S=0.75 to 1.25. In this range, anisotropy reaches a maximum value, about 1.65 (Fig. 10). The core flow can be called homogeneous only within 15mm from the centre. Both mean and turbulent velocities gradually increase outwards (Fig. 11).

The exit dimension of the burner is represented by the black rectangle at the bottom of the Fig. 11. One can indeed notice that horizontal velocities are characteristics of divergent flows and that they reach value of zero at the center of the burner. The differences on the edges as seen in the mean streamwise velocities are coming from slight differences in the swirls. However, the present investigation focuses mainly along the centerline of the jet and therefore those differences are not important. It should be noted that the central region presents a homogeneous flow. The extension of this homogeneous flow is similar to the one for which the actual mixture fraction is the one issued from the premixed section without dilution effects of the air swirls (Zimmer and Tachibana, 2005).

4.3 Integral length

There are four different ways to calculate integral length from raw data.

(1) Direct integration of auto-correlation;

$$\ell_1 = V \frac{\int_0^{\tau_0} \overline{v(t)v(t+\tau)}}{\overline{v(t)^2}} d\tau$$

where V, τ and τ_0 are the mean velocity, the time difference, and the elapsed time until auto-correlation becomes zero for the first time, respectively.

(2) Using a power spectrum peak position (Mydlarski & Warhaft, 1996);

See Appendix C.

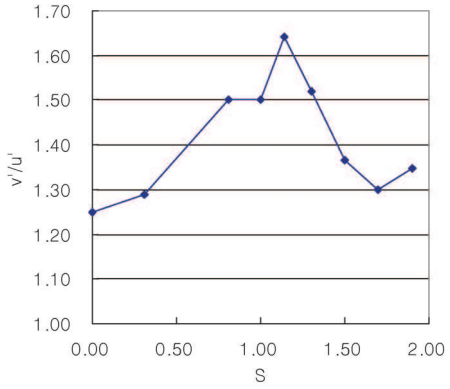

Fig. 10 Variation of anisotropy as S changes at y=10mm on the centerline.

(3) Using energy dissipation rate equation with an empirical coefficient (Mydlarski & Warhaft, 1996);

$$\ell_3 = 0.9v'^3/\varepsilon ,$$

$$\varepsilon = 15\nu \int_0^\infty \kappa^2 E_{vv}(\kappa) d\kappa = \frac{15\nu(2\pi)^2}{V^2} \int_0^\infty f^2 E_{vv}(f) df$$

where ε is the energy dissipation rate, E_{vv} the power spectrum density, κ the wave number, and f the frequency.

(4) PIV analysis;

$$\ell_{piv}(y_0) = \frac{\int_0^{\Delta y} \overline{v(y_0)v(y_0+y)}}{\overline{v(y_0)^2}} dy$$

where Δy means the distance where auto-correlation becomes zero for the first time.

The integral scale measurements using PIV are largely dependent on the grid used. Too big interrogation windows tend to overestimate the actual integral due to smoothing effects. Using small interroga-

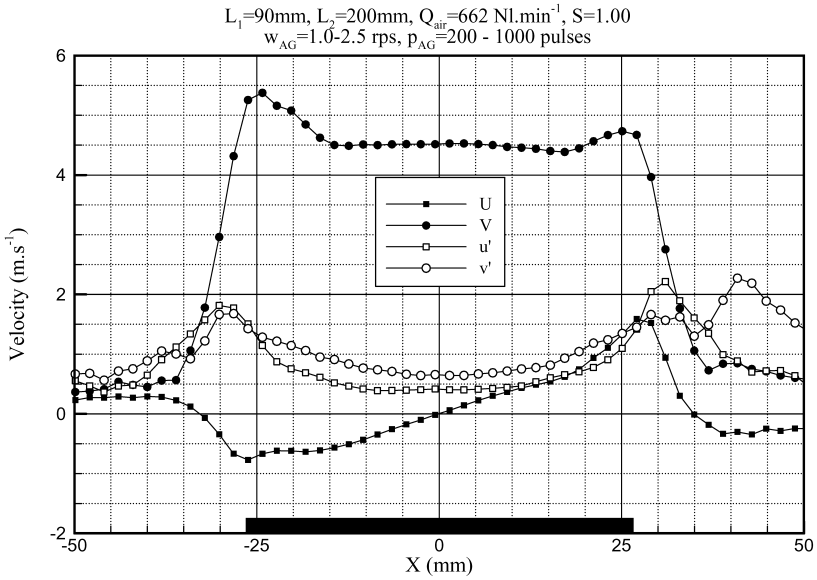

Fig. 11 Velocity profiles along transverse directions at y=10mm on the centerline.

tion window is not always possible to achieve good signal to noise ratio (see Appendix D for detailed discussion).

Fig. 12 shows the integral lengths measured at y=10mm from the nozzle exit, and interpreted by the above four methods. The PIV result is assumed to be correct because it is direct interpretation from velocity vector field. Then, integral length can be estimated to be about 15 to 20 mm for any swirl number under S=1.90. It has a small increase at around S=1.00, but does not vary much in general. The large deviation from the PIV of the results obtained using time series measurements by the hot-wire anemometer may indicate failure of Taylor's hypothesis based on the assumption of insignificant turbulent intensity, which is not the case in our experiments especially in case of large swirl numbers. The size of the largest turbulent structure cannot exceed a system dimension, here the inner diameter of the main pipe, 53mm. Considering that integral length means the largest eddy size, the result from the method (1) seems unreasonable. See Appendix C for explanation of why the yellow line is not available for large swirl flow rates.

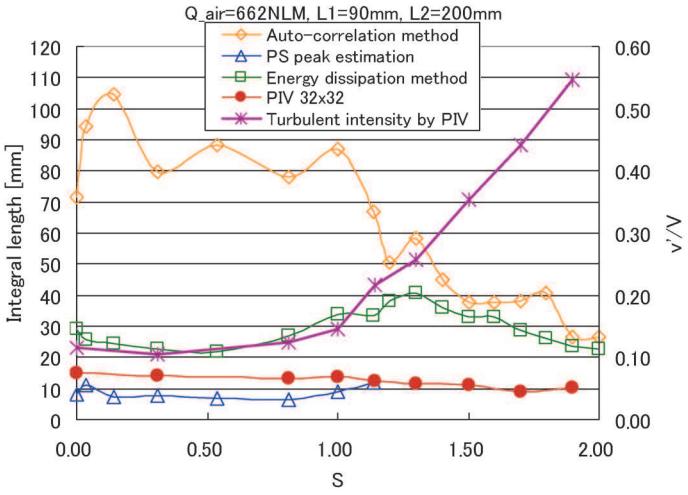

Fig. 12 Comparison of integral lengths obtained by various methods; Q_{air}=662NLM, ω_{AG}=1-2.5rps, p_{AG}=200-1000pulses

4.4 Turbulent energy spectra

Inertial subrange, which is denoted by -5/3 slope in energy spectra plots, has developed over one order of the frequency domain (Fig. 13). This width is less than two orders as first expected. However, the physical limitation on the eddy size referred to above should be considered. In the similar way to Appendix C, the inner diameter of pipe can be converted to the equivalent value in the frequency domain, about 11 Hz. Then, a frequency less than this does not have physical meaning in terms of eddies. So, there is small possibility for the inertial subrange to spread over two orders though one and half may be achievable. Consistently, Bedat & Cheng (1995), whose burner was 50.8 mm in inner diameter, reported that their turbulent flame contained the inertial subrange no wider than one order. And development of the inertial subrange seems not to depend on any specific

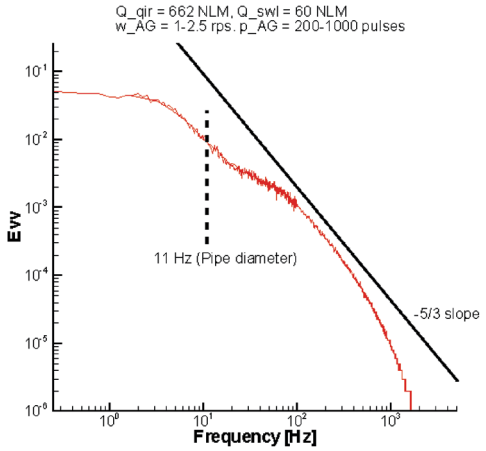

Fig. 13 Whole-range energy spectrum for a typical experimental condition

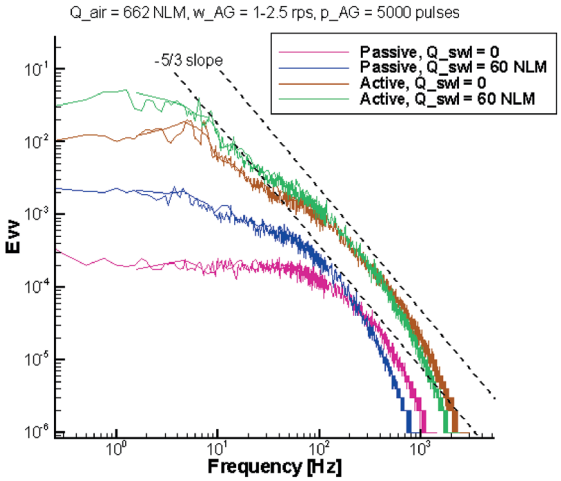

Fig. 14 Difference between active/passive grids, swirl/no swirl flow conditions

active grid condition much.

The active grid produces much stronger turbulent flow than the passive grid does (Fig. 14). Despite universal intensifying through all frequency ranges, low frequency energy level increases the most. This seems to be irrelevant to any specific active grid condition, but strongly depend on the existence of the active grid. When swirl flow is applied, the low frequency energy becomes stronger. But, high frequency energy weakens a bit. Another difference of passive-grid-generated turbulent flow is, whether there is swirl flow or not, that it does not have distinct inertial subrange.

In Fig. 15, as flow rate doubles, the energy level curves make parallel shifts upward. With the swirl number kept constant, it is not like Fig. 16 where the low frequency energy increases more than the higher frequency one. Higher flow rate may not be an effective way to widen the inertial subrange. However, in order to understand the effect of turbulent Reynolds number, further PIV experiments with higher flow rate need to be carried out. Four cases of different pipe lengths are tested for each flow condition. And there is small, but clear difference of energy level, especially, at the high frequency end; with a shorter pipe or at shorter downstream distance, the energy level is higher. It can be an evidence of decaying.

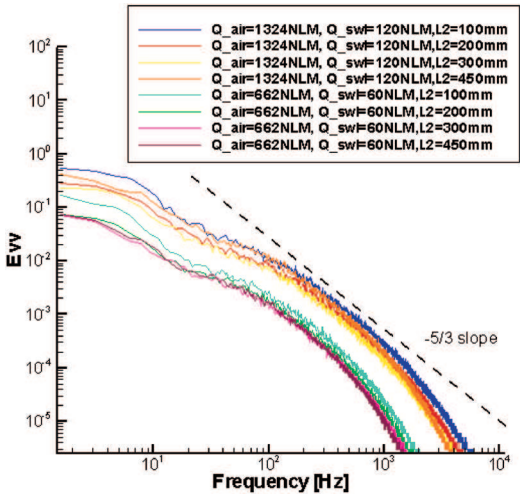

Fig. 15 Energy spectra for different flow rates with the same swirl number, and for different pipe lengths or distances downstream the active grid

4.5 Reacting flow

Combustion experiments using a methane/air mixture with 0.7 of equivalence ratio are carried out. While the mixture flow rate is fixed at 662 NLM, the swirl number changes from 1.0 to 1.9 systematically. For this range of swirl number, a blow-off seldom occurs. For those conditions, as the seeding is DEHS droplets, only fresh gases can be measured. The active grid is done using ω_{AG} ranging from 1000 to 2500 and p_{AG} from 200 to 1000.

Important parameters from Mie scattering images are not only the velocity but also the position of the flame front. Due to the burning of the droplets, it is possible to distinguish burnt and unburnt zones. The assumption being here that vaporization of droplets coincide with the flame front. Due to limited spatial resolution of this method (relying on averaged inten-

sity over a region), the progress variable c is computed on an interrogation size with spacing of 0.5mm. A typical instantaneous image obtained during PIV tests is displayed in Fig. 16. One can clearly notice the boundary between fresh and burnt gases. Fresh gases are the regions where the mean intensity is higher than a threshold (in the present case the threshold was set at 20% of the full scale of the CCD). Determining for each image the windows considered as fresh gases, it is possible to compute the PDF of being in burnt state; therefore to provide a spatial distribution of the progress variable c. A value of c equals to unity means that burnt gases are always present in this region.

Looking at a two-dimensional distribution of the progress variable shows, as seen in Fig. 17, that the flame has a slight curvature in the center for small values of c, whereas for higher values (higher than 0.50), its shape becomes flat.

Typical output for a nozzle length of 90mm is displayed in Fig. 18 for points along the central axis. For an increase of swirl number, the progress variable distribution tends to move closer to the burner, which is in agreement with previous evaluations.

To discuss the lift-off height of the flame, it is possible to use the height as for c=0.5 which is the most probable position of the flame front. Typical variation is shown in Fig. 19 where one can notice that similarly to passive grid cases (Tachibana and Zimmer, 2005), a lower nozzle leads to a stabilization's point closer to the exit of the burner for an identical initial swirl number.

Fig. 16 Typical Mie scattering image

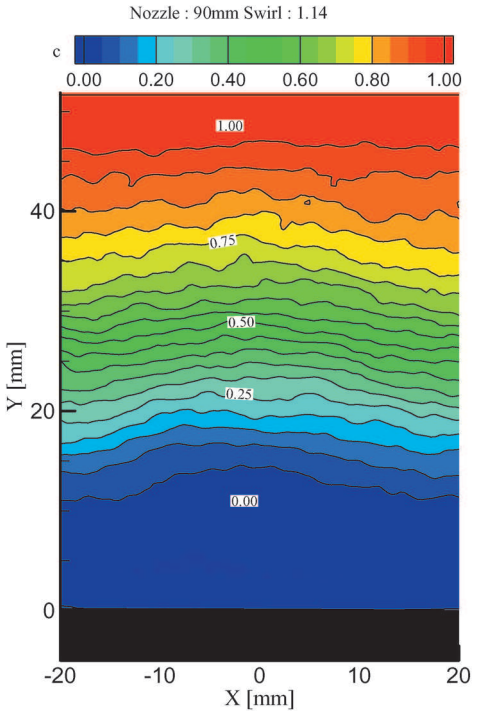

Fig. 17 Two-dimensional distribution of progress variable

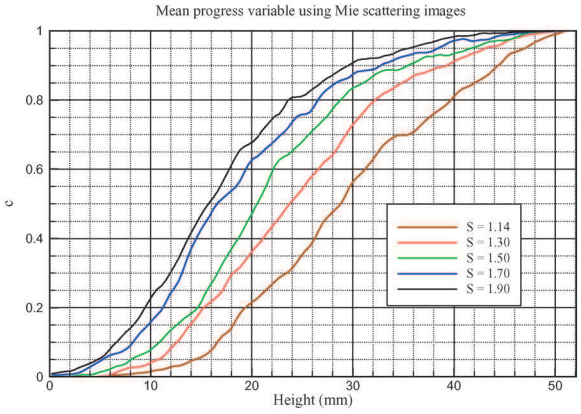

Fig. 18 Mean progress variable for different swirl (L=90mm)

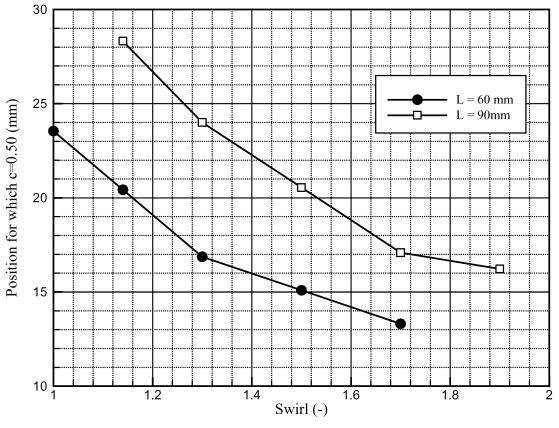

Fig. 19 Variation of c=0.50 with swirl numbers

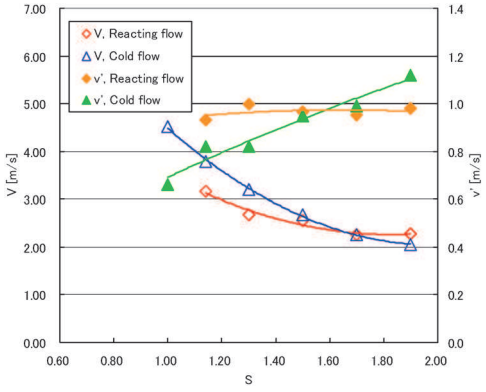

Fig. 20 Comparison of velocity variation for reacting and cold flows; for unburnt area

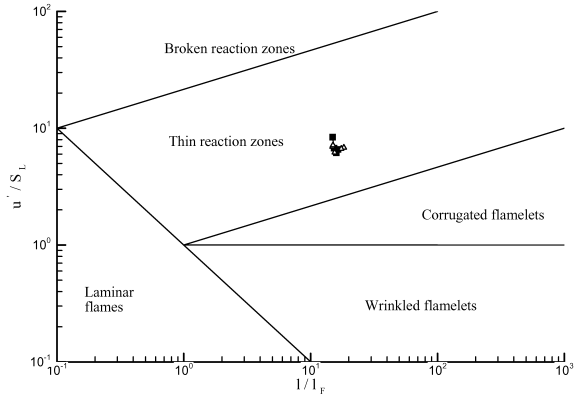

Fig. 21 Premixed flame regime diagram, Peters (2000); for y=5mm at centre

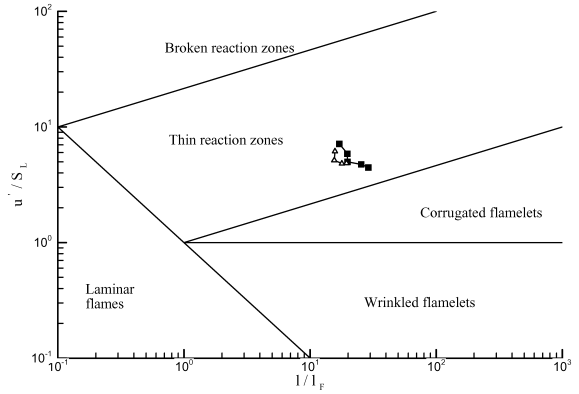

Fig. 22 Variation within the combustion diagram as function of PIV interrogation size

Compared to the same operating conditions with cold flow in Fig. 9, velocity changed less rapidly. The data for reacting flow in Fig. 20 were of the unburned area, taken 10mm above the exit of the burner along the centerline.

In order to calculate turbulent Karlovitz number, a laminar flame propagating velocity, s_L, and a laminar flame thickness, l_F, are necessary. l_F is defined as follow by Peters (2000);

$$\ell_F = \frac{(\lambda / c_p)_0}{(\rho s_L)_u}$$

where λ is a thermal conductivity. Here, the subscript zero means the position where the concentration of hydrogen radical becomes its highest value. s_L can be obtained using CHEMKIN II code with PREMIX module, and GRI-MECH 3.0, assuming inlet temperature and pressure as 298 K and 1 atm. And, other thermodynamic properties are based on CHEMKIN data. Then, l_F and S_L are 0.269 mm and 0.232 m/s, respectively. The definition of turbulent Karlovitz number is provided by Peters (2000);

$$Ka = \left(\frac{v'}{s_L}\right)^{3/2} \left(\frac{\ell_F}{\ell}\right)^{1/2}$$

With the data measured at x=0 and y=5mm (always in fresh gases), Ka is higher than 1.0 for any tested swirl numbers so that it can be said the flames represent the thin reaction zones flame, as shown in Fig. 21.

But it should be said that the correlation curves from PIV analysis do not always converge to zero. Hence, the integral length, as well as Ka, can have different values with respect to analysis schemes. For the present calculation, no extrapolation is applied to the correlation curves. However, those changes would not influence the proper estimation of the turbulent combustion regime. To validate this assertion, two cases are computed for different PIV interrogation sizes and therefore spatial resolution, from 128×128 down to 24×24 pixel × pixel (representing respectively 3.5 and 0.65 mm × mm). Results are shown in Fig. 22. One can notice small changes in the exact position within this diagram as lower points for each series represent the coarser interrogation size measurements, whereas the highest point is for the finer grid. After some points, the grid shall not be refined as what comes out may be more noise than real information and therefore one should not rely on those measurements to educe the combustion diagram.

One may conclude from the PIV experiments that the flames generated by the active grid experiments are laying in the thin reaction zones regime, which was the target of developing the active grid.

5. Summary

The Makita-style active grid was designed to complement the present LSB to produce stronger turbulence. Through the parametric experimentation, adequate active grid and flow conditions were found. The turbulent energy spectra in active grid cases show higher energy density over the whole range and wider inertial subrange than those of passive grid cases. Even though the generated flow often contained large low frequency peaks, possibly induced by the grid movements, it was shown that these peaks can be controlled by adjusting the grid options. For the swirl number range used in the reacting flow experiments, the turbulent fluctuation reached about 1.0 m/s while it was successful to keep the integral length under 20 mm. Consequently, the resulting flames enter the thin reaction zones regime.

References

[1] Bedat, B., and Cheng, R. K. (1995) "Experimental study of premixed flames in intense isotropic turbulence", *Combustion and flame vol. 100*, pp. 485-494.

[2] Cheng, R. K. (1995) "Velocity and scalar characteristics of premixed turbulent flames stabilized by weak swirl", *Combustion and flame vol. 101*, pp. 1-14.

[3] Cheng, R. K., and Fable, S. A. (2001) "Development of a low swirl injector concept for gas turbines", *Proceedings of IJPGC 2001*.

[4] Johnson, M. R., and Cheng, R. K. (2003) *Proc. of The 19th International Colloquium on the Dynamics of Explosions and Reactive Systems in Hakone, Japan*.

[5] Kang, H. S., Chester, S. and Meneveau C. (2003) "Decaying turbulence in an active-grid-generated flow and comparisons with large-eddy simulation", *J. Fluid Mech. vol. 480*, pp. 129-160.

[6] King, L. V. (1914) "On the convection of hear from small cylinders in a stream of fluid : Determination of convection constants of small platinum wires with applications to hot-wire anemometry", *Phil. Trans. Roy. Soc. A214*, pp, 373-432.

[7] Larssen, J. V., and Devenport, W. J. (2003) "Interaction of large scale homogeneous turbulence with a cascade of flat plates", *AIAA-2003-0424*.

[8] Makita, H. (1991) "Realization of a large-scale turbulence field in a small wind tunnel", *Fluid Dynamics Research vol. 8*, pp. 53-64.

[9] Mehta, R. D. and Hoffmann, P. H. (1987) "Boundary layer two-dimensionality in wind tunnels", *Experiments in Fluids, vol. 5*, p. 358.

[10] Mydlarski, L., and Warhaft, Z. (1996) "On the onset of high-Reynolds-number grid-generated wind tunnel turbulence", *J. Fluid Mech. vol. 320*, pp. 331-368.

[11] Peters, N. (2000) "Turbulent Combustion", *Cambridge University Press., Cambridge, UK*, 304pp.

[12] Poorte, R. E. G., and Biesheuvel, A. (2002) "Experiments on the motion of gas bubbles in turbulence generated by an active grid", *J. Fluid Mech. vol. 461*, pp. 127-154.

[13] Tachibana, S., Zimmer, L. and Suzuki, K. (2004) "Study on turbulent premixed flames of a low-swirl burner", *Journal of the Combustion Society of Japan vol. 46*, pp. 153-159.

[14] Tachibana, S. and Zimmer, L. (2005) "Effect of Swirl on the Stability of a Lifted Flame Sustained by a Low-Swirl Burner", *20th International Colloquium of the Dynamics of Explosion and Reactive Systems*, Montreal, Canada. (http://www.galcit.caltech.edu/~jeshep/icders/program.php#103)

[15] Videto, B. D., and Santavicca, D. A. (1991) "A turbulent flow system for studying turbulent combustion processes", *Combust. Sci. Technol. vol. 76*, pp. 159-164.

[16] Zimmer, L., Tachibana, S. and Suzuki, K. (2004) "Conditional Velocity measurements in premixed flames", *9th French speaking congress on laser Velocimetry*, Brussels, 14-16 September

[17] Zimmer, L. and Tachibana, S. (2005) "Laser Induced Plasma Spectroscopy for local composition measurements inside a low swirl burner", *20th International Colloquium of the Dynamics of Explosion and Reactive Systems*, Montreal, Canada. (http://www.galcit.caltech.edu/~jeshep/icders/program.php#68)

Appendix A : Detailed design of the active grid

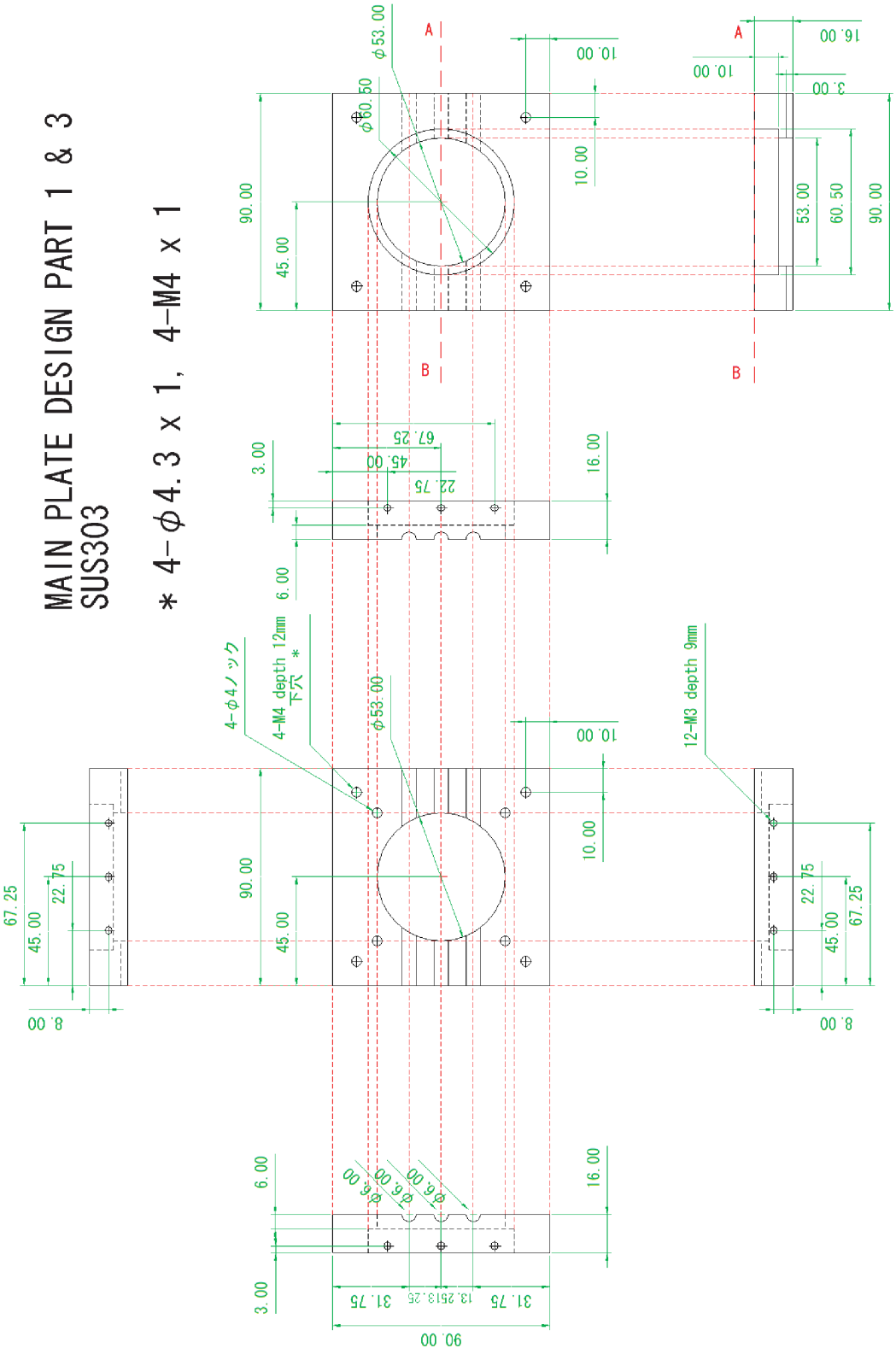

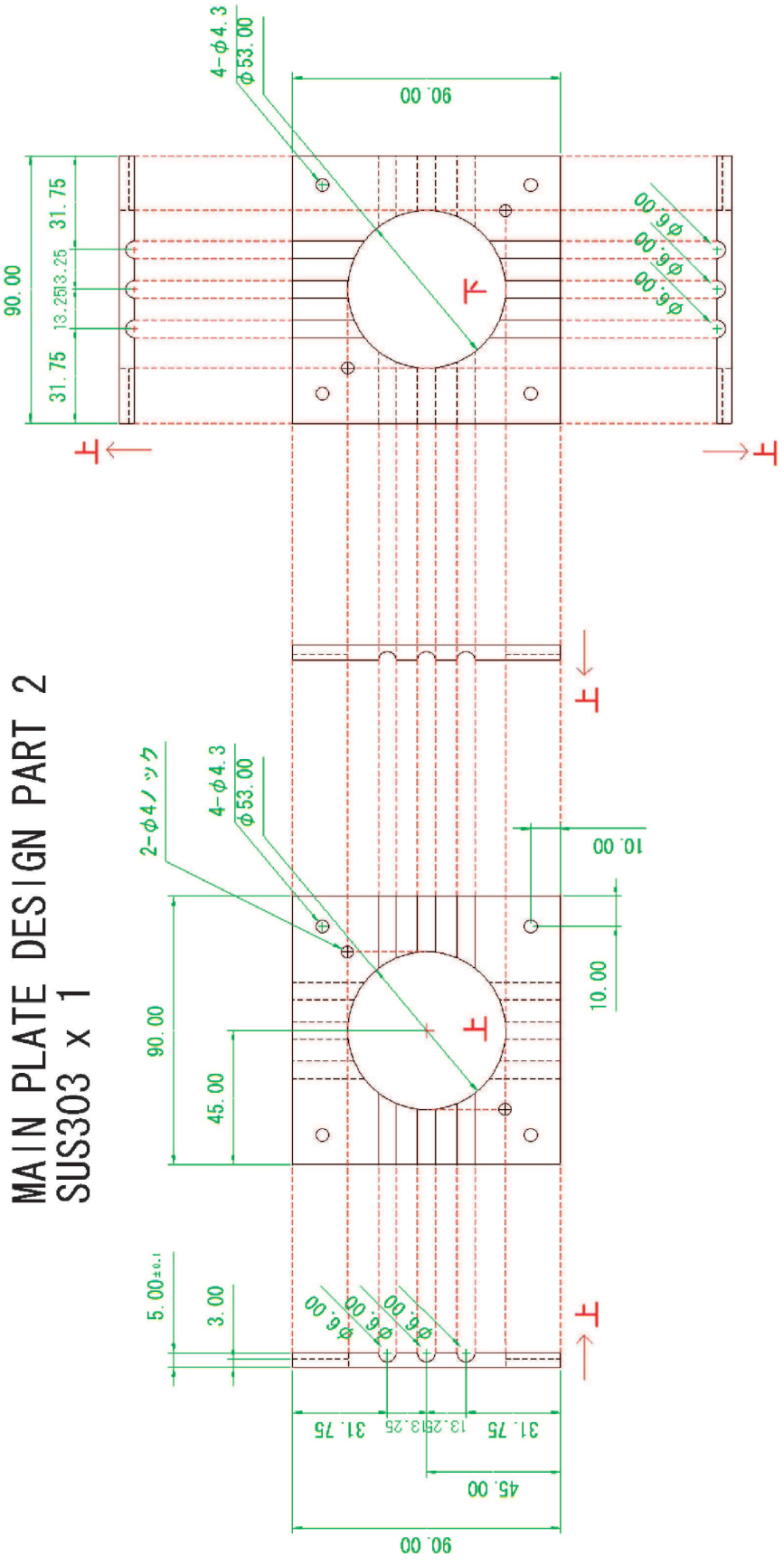
MAIN PLATE DESIGN PART 2
SUS303 x 1
4-φ4.3
φ53.00
90.00
31.75
13.25
13.25
31.75
90.00
φ6.00
φ6.00
φ6.00
φ6.00
2-φ4ノック
4-φ4.3
φ53.00
10.00
10.00
90.00
45.00
5.00±0.1
3.00
φ6.00
φ6.00
φ6.00
φ6.00
31.75
13.25
13.25
31.75
45.00
90.00

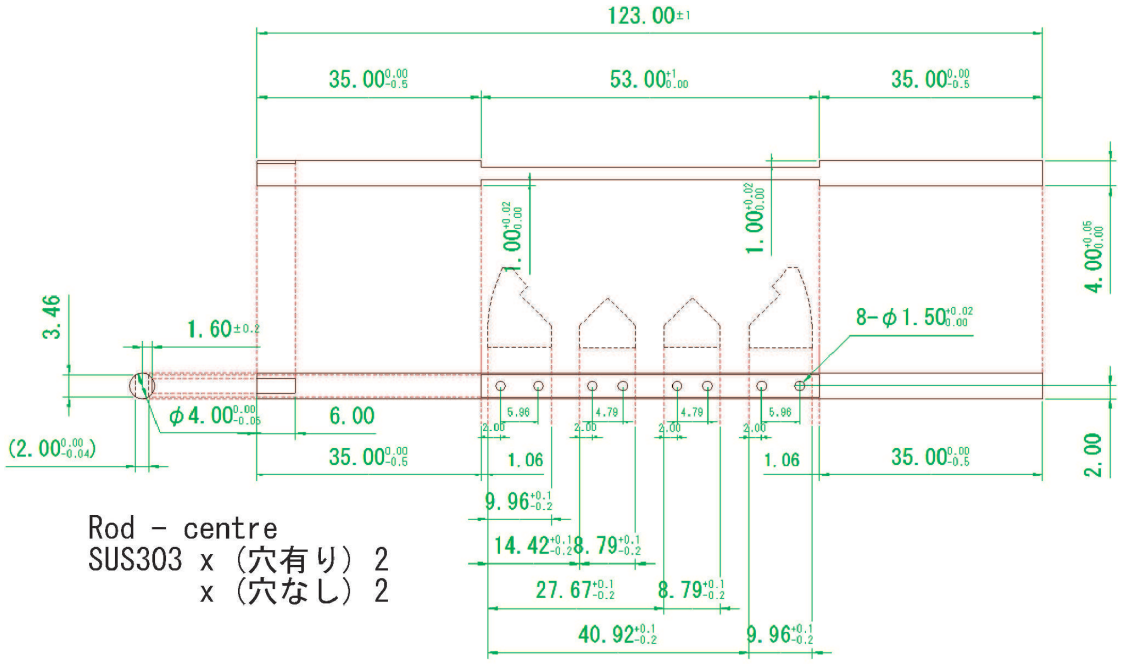
123.00±1
35.00
53.00
35.00
1.00
1.00
4.00
3.46
1.60±0.2
8-φ1.50
φ4.00
6.00
(2.00)
35.00
1.06
1.06
35.00
2.00
9.96
14.42
8.79
27.67
8.79
40.92
9.96
Rod - centre
SUS303 x (穴有り) 2
x (穴なし) 2

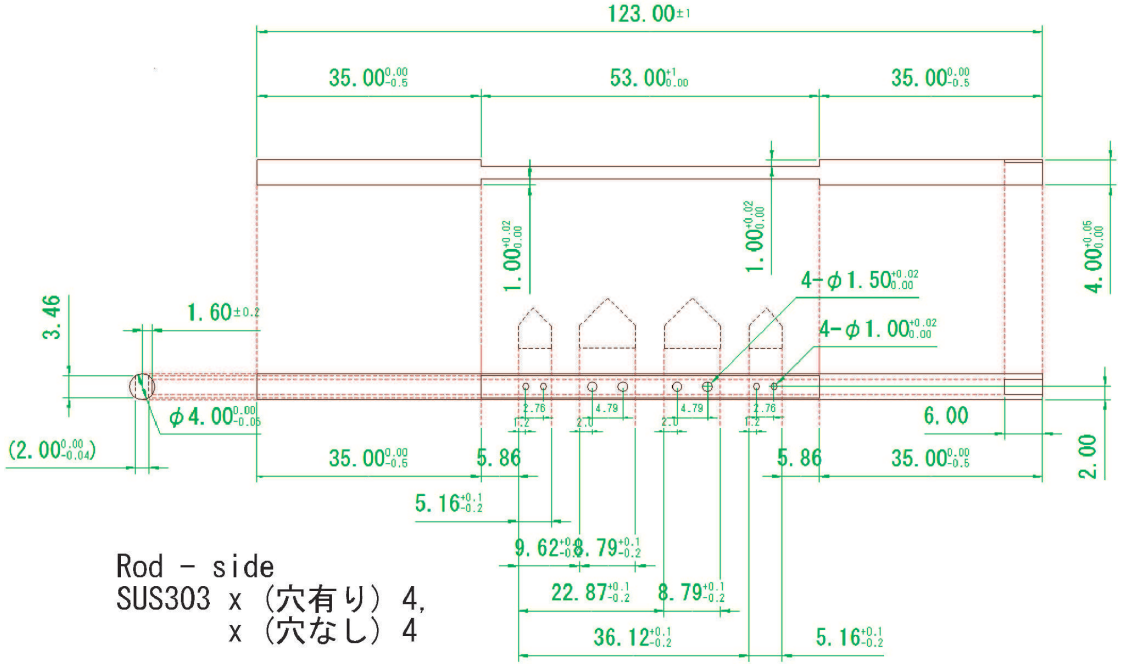
123.00±1
35.00
53.00
35.00
1.00
1.00
4.00
3.46
1.60±0.2
4-φ1.50
4-φ1.00
φ4.00
6.00
(2.00)
35.00
5.86
5.86
35.00
2.00
5.16
9.62
8.79
22.87
8.79
36.12
5.16
Rod - side
SUS303 x (穴有り) 4,
x (穴なし) 4

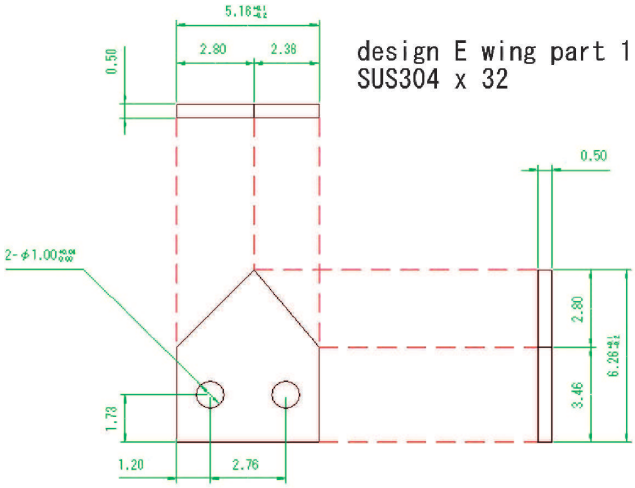
design E wing part 1
SUS304 x 32
5.16
2.80
2.36
0.50
0.50
2-φ1.00
2.80
6.26
3.46
1.73
1.20
2.76

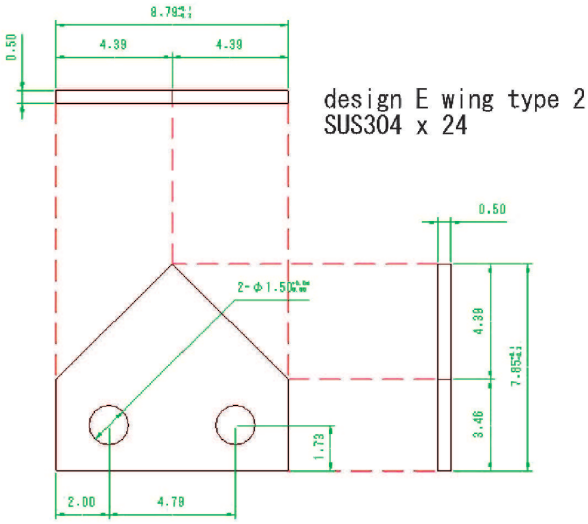
design E wing type 2
SUS304 x 24
8.78
4.39
4.39
0.50
0.50
2-φ1.50
4.39
7.85
3.46
1.73
2.00
4.78

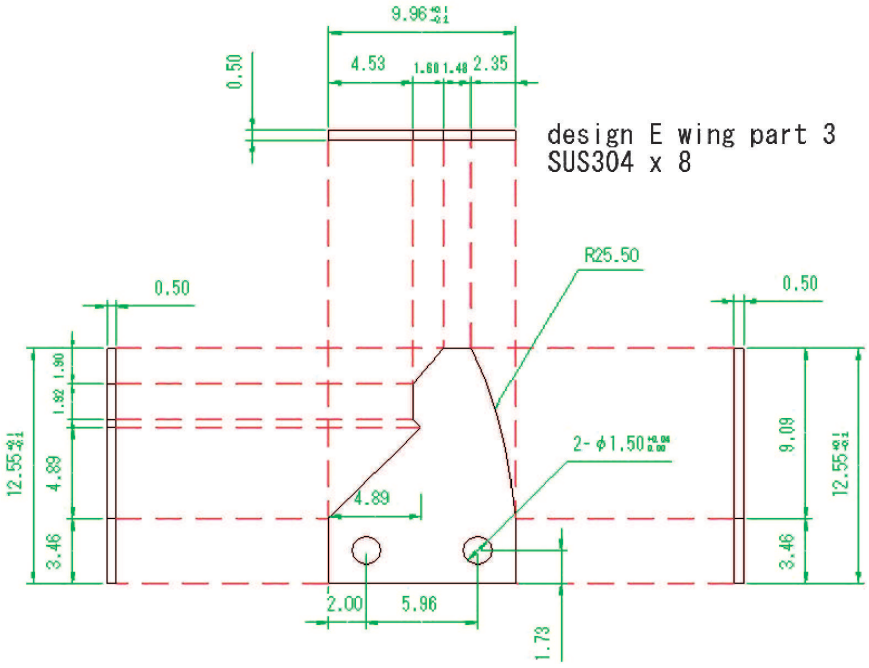
design E wing part 3
SUS304 x 8
9.96
4.53
1.80
1.48
2.35
0.50
R25.50
0.50
0.50
12.55
1.80
1.82
4.89
3.46
2-φ1.50
4.89
9.09
12.55
3.46
2.00
5.96
1.73

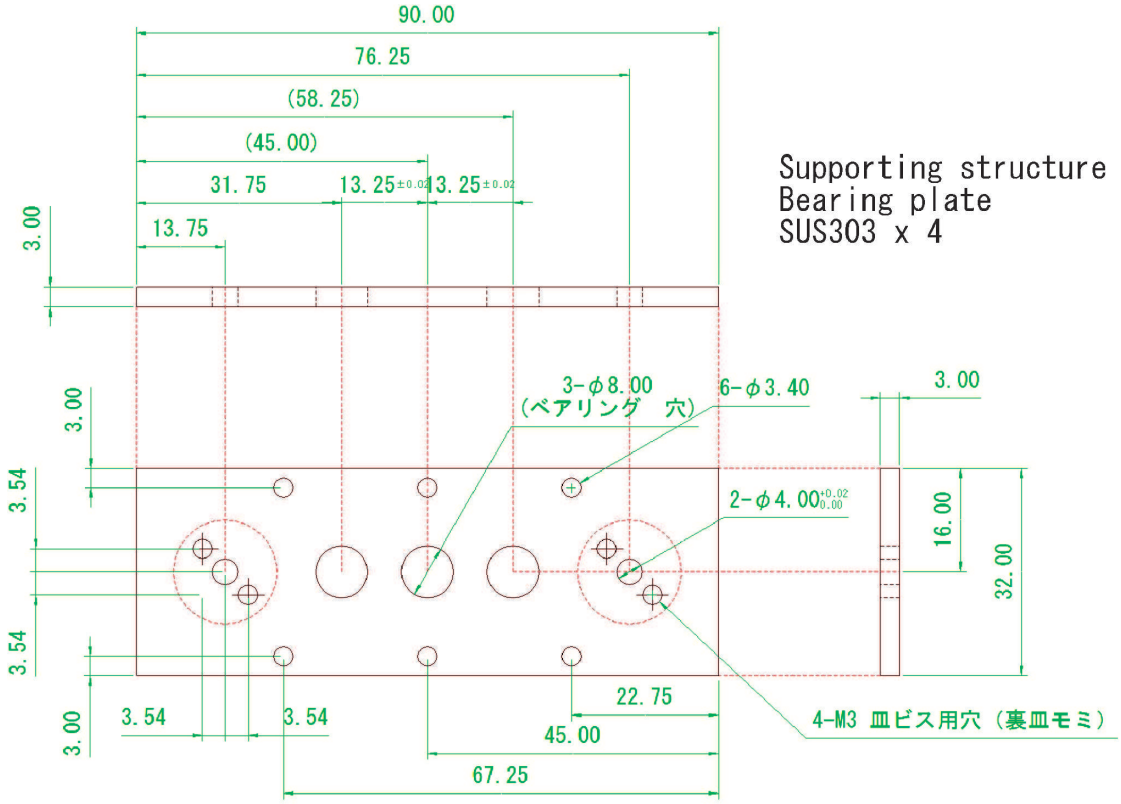
90.00
76.25
(58.25)
(45.00)
31.75
13.25±0.02
13.25±0.02
13.75
3.00
3.00
3.54
3.54
3.00
3-φ8.00
(ベアリング 穴)
6-φ3.40
3.00
2-φ4.00+0.02 0.00
16.00
32.00
3.54
3.54
22.75
45.00
67.25
4-M3 皿ビス用穴（裏皿モミ）
Supporting structure
Bearing plate
SUS303 x 4

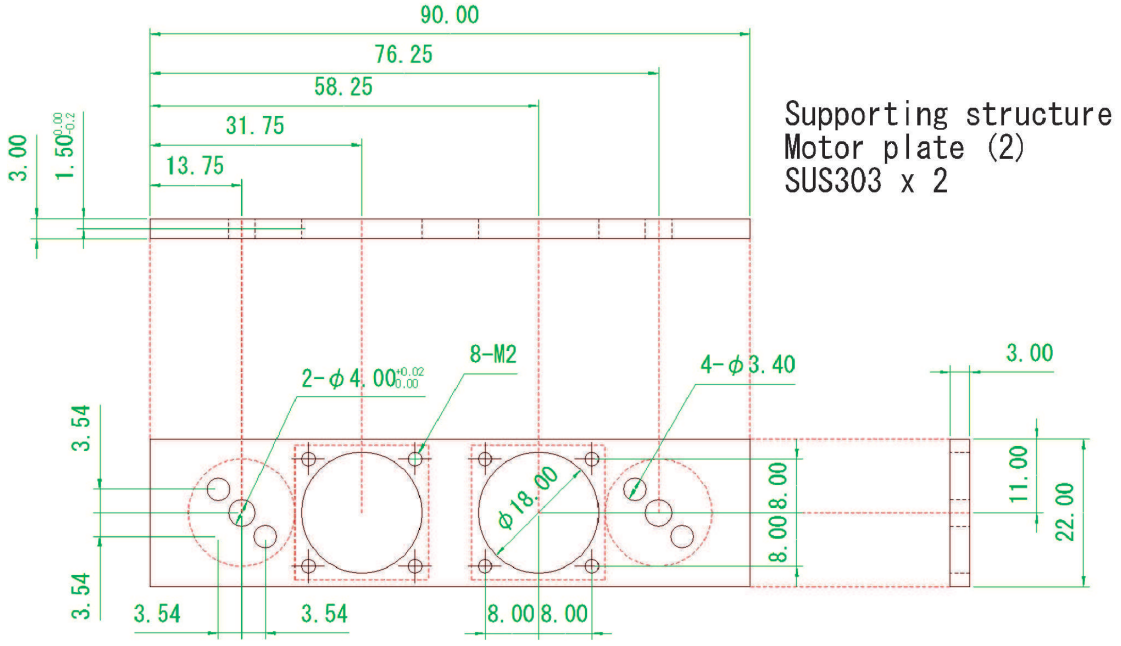
90.00
76.25
58.25
31.75
13.75
3.00
1.50+0.00 -0.2
2-φ4.00+0.02 0.00
8-M2
4-φ3.40
3.00
3.54
3.54
φ18.00
8.00
8.00
11.00
22.00
3.54
3.54
8.00
8.00
Supporting structure
Motor plate (2)
SUS303 x 2

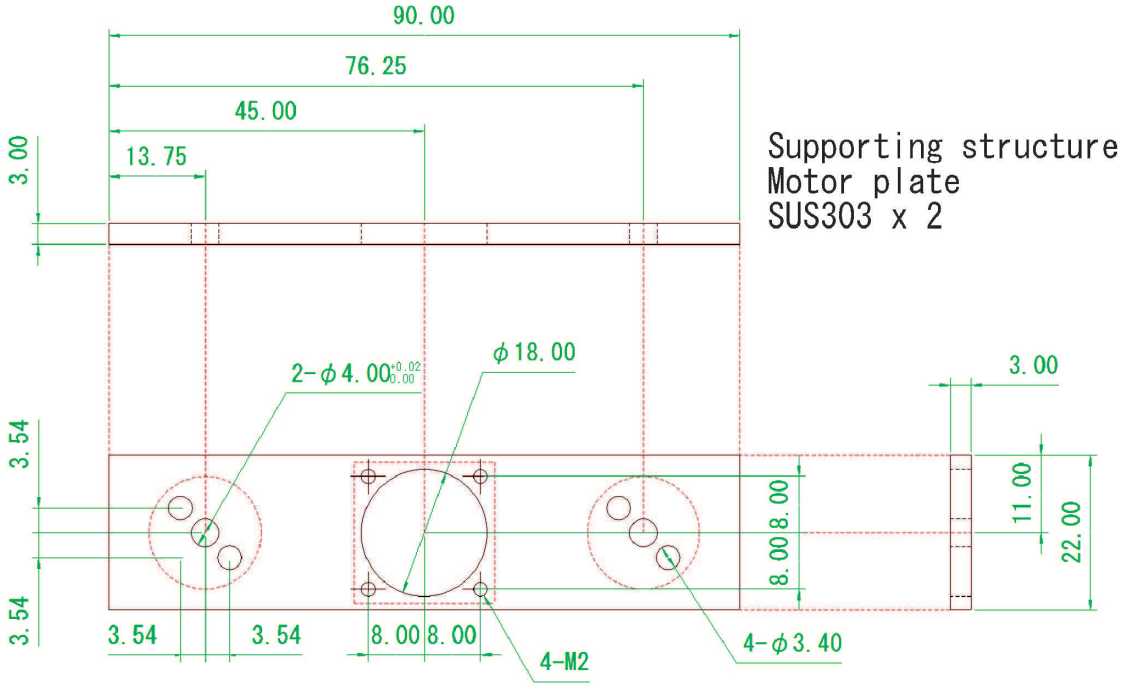
90.00
76.25
45.00
13.75
3.00
Supporting structure
Motor plate
SUS303 x 2
2-φ4.00
φ18.00
3.00
3.54
3.54
8.00
8.00
11.00
22.00
3.54
3.54
8.00
8.00
4-M2
4-φ3.40

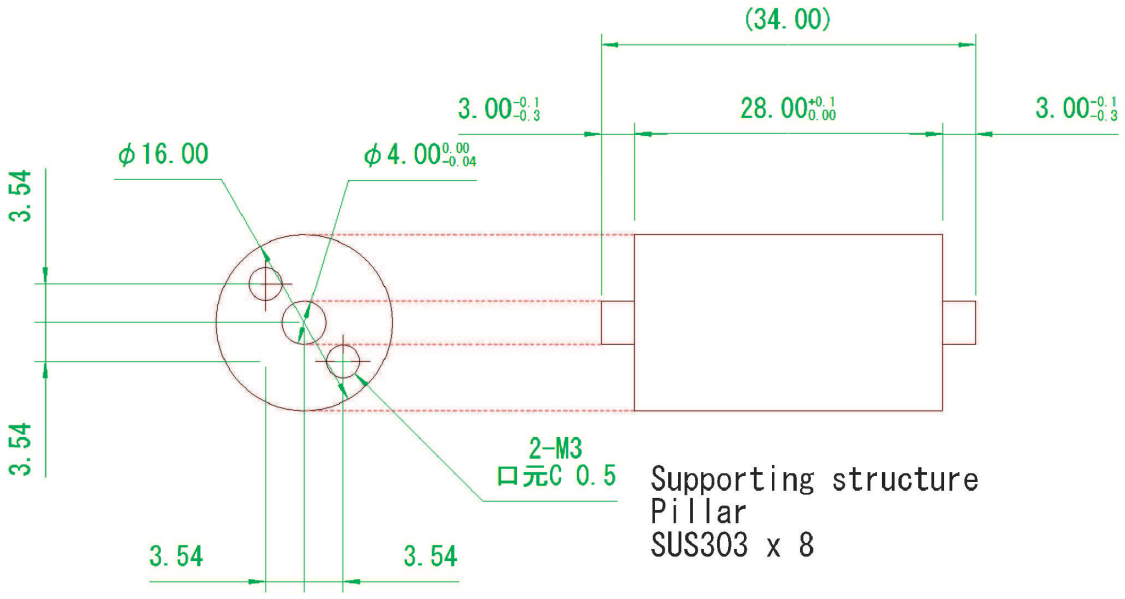
(34.00)
3.00
28.00
3.00
φ16.00
φ4.00
3.54
3.54
2-M3
C0.5
Supporting structure
Pillar
SUS303 x 8
3.54
3.54

Appendix B : Integral part of the motor controlling LabVIEW programme

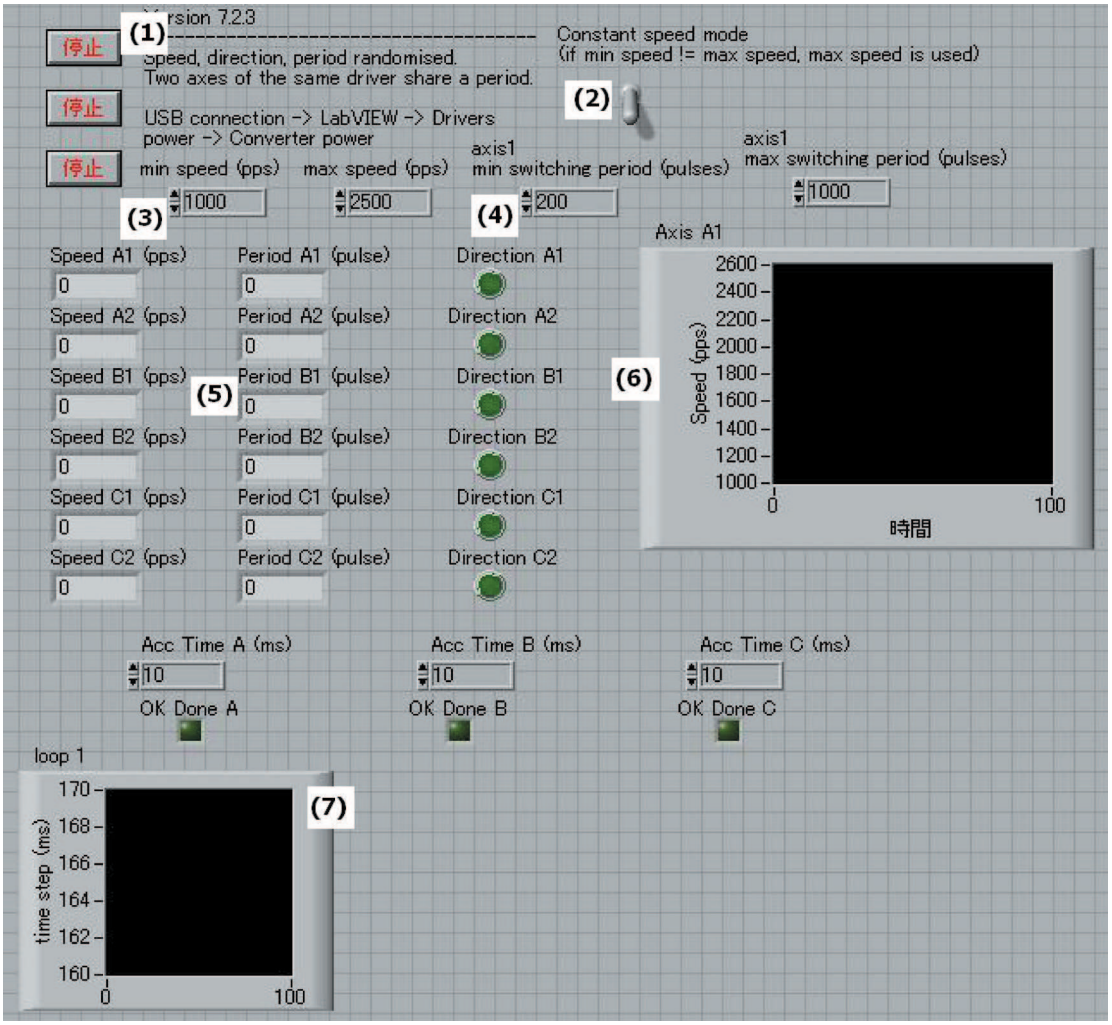

Figure B.1 Front Panel of main user interface function

(1) Stop buttons for three drivers

(2) Constant speed mode option button:
If this is ON, the maximum speed setting is applied as a constant rotating speed.
If this is OFF, a rotating speed is decided randomly in the specified range.

(3) Speed range setting box
The unit is pulse per second, where a pulse means 0.36 degree.

(4) Direction switching period range setting box
The unit is pulses.

(5) Display of rotating speed, direction, and period of all axes

(6) Display of rotating speed history of the axis number 1
It is for checking if random function works properly.

(7) Display of time that one stage of the whole commanding loop takes to be executed

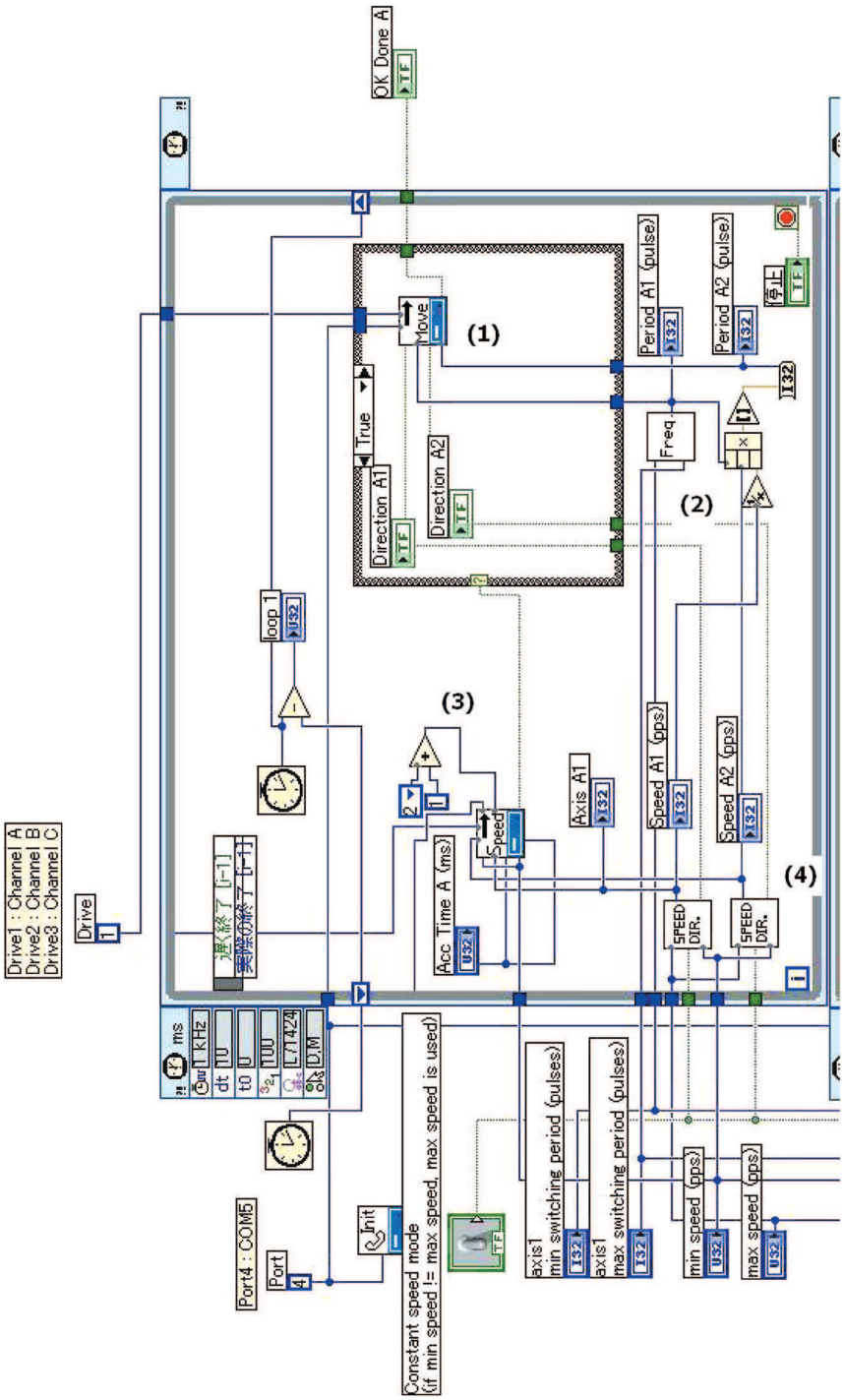

Figure B.2 Part of the block diagram of main user interface function

(1) Compose and send 'move' commands to the drivers.

(2) Randomly decide switching period for the first axis. Then, adjust the second period so that two axes having different rotating speeds stop at the same time.

(3) Set the decided speed conditions to motors

(4) Randomly decide rotating speed and direction.

Appendix C : Estimation of integral length scale from energy spectra plot

Mydlarski and Warhaft (1996) suggested that a peak in energy spectra determined by multiplying the power spectra density by wave number k provides a very good estimate of the integral scale of the turbulence. In this way, a peak frequency read from a frequency versus frequency*power spectra density plot can be converted to length scale by the following equation,

$$2\pi f = Vk = V/\ell$$

where f, V, k are frequency, mean velocity, wave number or reciprocal of length scale. Estimated integral lengths by this method are fairly constant, l=15 mm, regardless of active grid options for swirl number 1.14, while they are much deviated from the results obtained by auto-correlation method (see below).

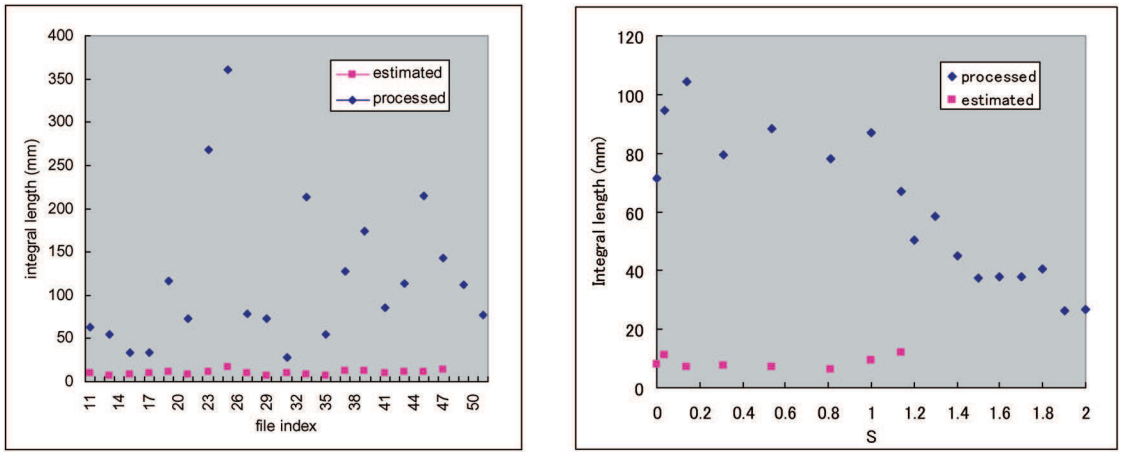

(Left) Integral length for various AG conditions with S of 1.14, and (Right) Integral length for various S when the active grid is on

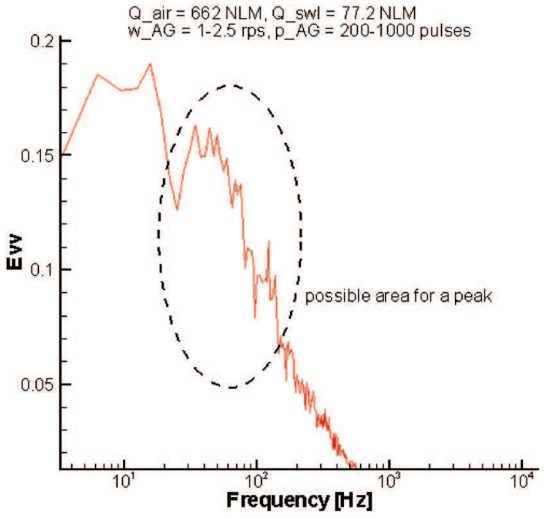

However, this method is ineffective for higher swirl numbers. It is because low frequency response becomes so large due to strong swirl flow that peaks cannot be clearly seen on energy spectra.

Strong low frequency response may cover 'real' peaks

Appendix D: Integral length scales measurements using Particle Image Velocimetry data

General processing from PIV data to integral length scale measurement

Using PIV allows to measure at different point the integral length scales for the two components. Hence, both streamwise and transverse integral can be obtained. It seems obvious that the transverse integral is bounded to the radius inside the burner. However, as measurements are done 10mm above the exit, values may increase due to the opening of the jet.

The principle of measurement of the integral length is the two-point correlation method.

$$f(y) = \overline{v'(y_0)v'(y_0+y)} \Big/ \overline{v'(y_0)^2}$$

$$l_{yy} = \int_0^\infty f(y)dy$$

Typically 500 images are used to obtain the integral length scales. Before presenting a summary of the results for the active grid, an important remark is done as far as the integral length scale is concerned. As shown in Fig. 1, one can see that some conditions (in this case without swirl) do not lead to bounded values of the integral as the correlation coefficient never becomes negative for the present field of view chosen (115mm above the burner).

The problem becomes more drastic in reacting conditions, as the particles do burn and therefore no measurements are possible in burnt gases. It may be possible to recover the information by assuming an exponential decay for the correlation coefficient. Typical examples of such process are displayed in Fig. 2-Fig. 5. The horizontal axis corresponds to the spatial distance between the points for which correlation coefficient is computed. The absolute values of the coefficients are plotted along the vertical axis. The example chosen corresponds to a swirl number of 1.90 and for a nozzle length of 90mm and 10mm above the exit of the burner.

The curve does represent the actual measured correlation coefficient, whereas dots correspond to the exponential fit based upon the first points in space. One can notice that using 3 points leads certainly to a sharp decrease of the correlation coefficients and therefore will tend to underestimate the integral length scale. As reference, the inferred scales are given above each figure. One can hence see that exponential fit based on 3 points leads to an estimation of 3.06mm whereas 5 points gives 4.46mm. When looking at the exponential fitting curves, one may notice that fitting done with more than 6 points clearly overestimate the actual integral length scale (as shown in Fig. 5 for instance with 8 points). In this figure, the part for which enough statistics could be gathered (smooth profile) is clearly below the ex-

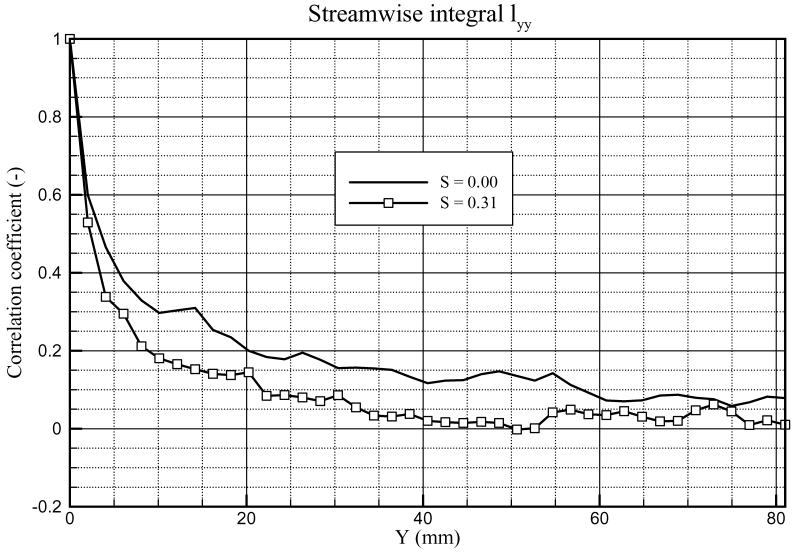

Fig. 1 Typical correlation for active grid

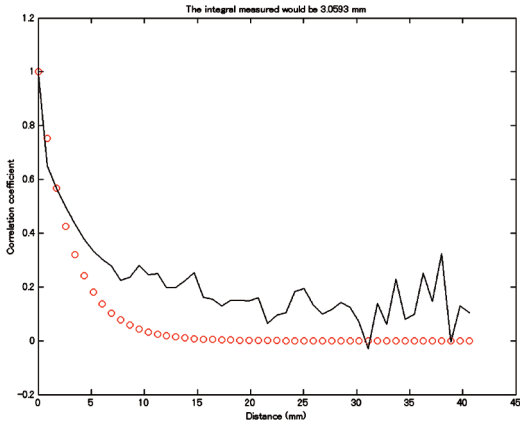

Fig. 2 Exponential fit with 3 points only

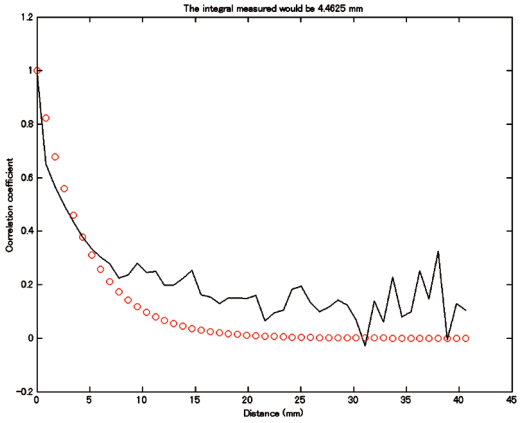

Fig. 4 Exponential fit with 5 points only

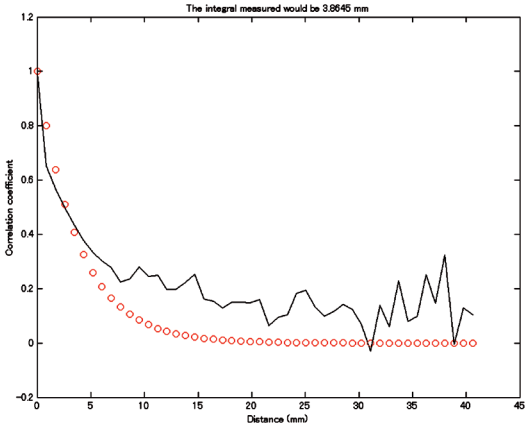

Fig. 3 Exponential fit with 4 points only

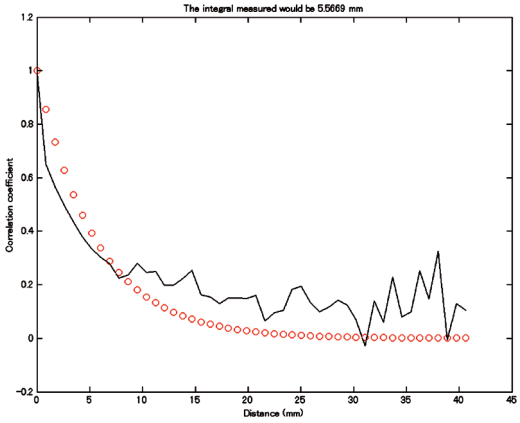

Fig. 5 Exponential fit with 8 points only

ponentially fitted curve. It is possible to determine a parametric study on the influence of the number of points on the final results to see how sensitive the computation is to the size of the domain used. A summary of three different swirl numbers for a length of 90mm is given in Fig. 6. One can see that no convergence is reached as the integral length scale increases monotically with an increase of the number of points used for the exponential fitting procedure.

Sub-grid scale filtering effects

PIV presents filtered measurements of instantaneous velocity within a plane of the flow. The filter size depends directly on the size of the mesh upon which correlation is done. Having a coarse mesh will indeed smooth the data and PIV would not be able to get all the features of the turbulence. This sub-grid filter effect will affect the measurements of turbulence levels. As those are used in the computation of the integral length scales, it will also be strongly affected by the size of the window used. However, it is possible to try to evaluate the part missed and therefore applying correction on the actual measurements. To properly evaluate the sub-grid filtered information, the computation over several grid resolutions is required. Using multiple of 2 for the window sizes allows utilizing fast Fourier transform algorithms. However, to also have the results on grids of 48×48 or 24×24, FFT algorithms cannot be used and therefore the processing time required is becoming a crucial issue.

The higher the spatial resolution, the more accurate the integral length scale measurement would be. A too rough spatial resolution will tend to overestimate the actual integral length scale. Therefore, the ratio between true and measured integral length scale should be less than unity. Increasing spatial resolution will tend to reduce the integral length scale measurement. On the other hand, turbulent fluctuations will tend to increase. The integral length scale is as-

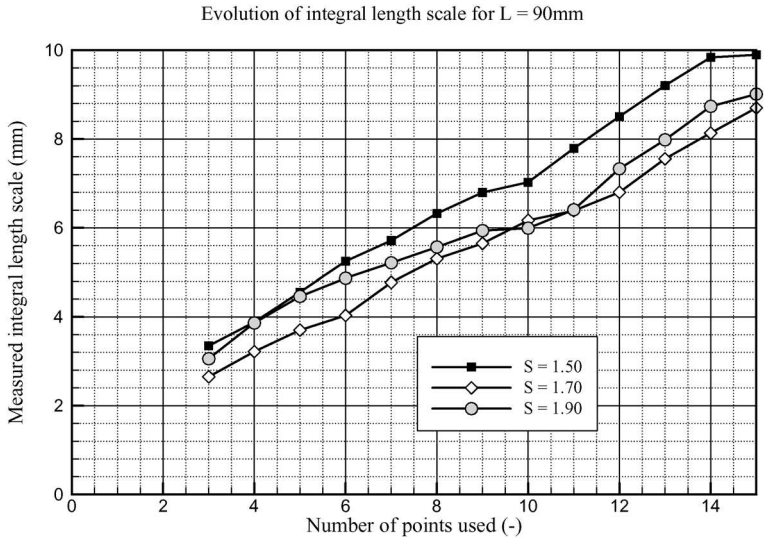

Fig. 6 Evolution of integral length as function of exponential fit domain

Therefore for the cases that were not bounded, a fitting procedure with 5 points was used to determine the actual integral length scale

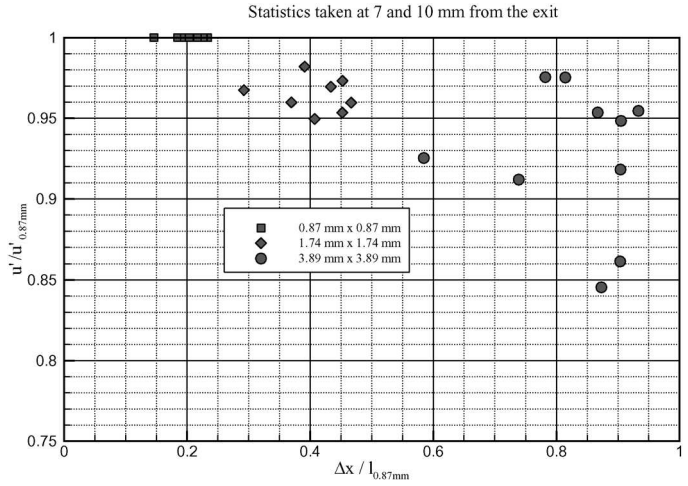

Fig. 7 Ratio between turbulent velocities as function of spatial resolution

sumed to be correctly measured when using the smallest interrogation cell. Therefore for each window size, the ratio between the correlation window and the integral length scale can be computed. Afterwards, it is also possible to compute the ratio between the turbulent velocity and a "true" turbulent velocity, as measured with the lowest window size. A typical example of the changes in actual values is depicted in Fig. 7 for turbulent velocity measurements. One can notice that the lowest ratio between integral length and spatial resolution is of the order of 0.2. Little changes were obtained when using the smallest interrogation size and therefore one may estimate that the convergence of the integral length scale in terms of spatial resolution has been achieved.

Similar results may be obtained for the integral length scale measurements as function of the spatial resolution. This time the ratio between the true integral (measured with the highest spatial resolution) and the integral as measured with a given spatial resolution is plotted versus the ratio between the spatial resolution and the smallest integral length scale measured (see Fig. 8). One can also notice that the ratio tends to unity for spatial resolution of 20% of the integral length scale. Using smaller spatial resolution tends to overestimate the integral length

scale more drastically than what has been seen for the turbulent velocities as current changes may be of the order of 40%.

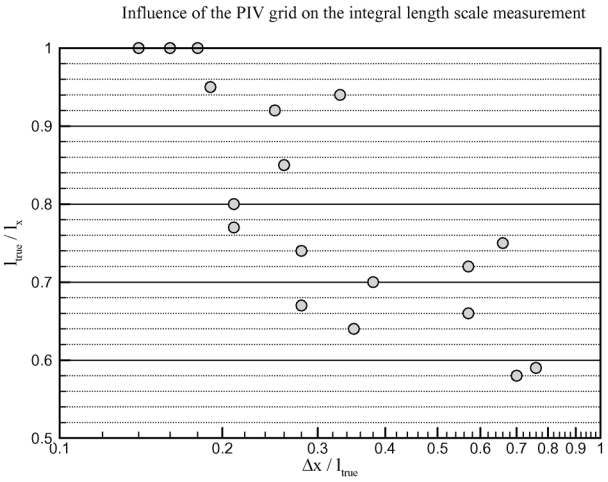

Fig. 8 Ratio between integral length scales as function of spatial resolution

JAXA Research and Development Report JAXA-RR-05-055E

Date of Issue : March 31, 2006
Edited and Published by : Japan Aerospace Exploration Agency
7-44-1 Jindaiji-higashimachi, Chofu-shi, Tokyo 182-8522, Japan
URL : http://www.jaxa.jp/
Printed by : Jitsugyo-kohosha Co.,Ltd.

JAXA Research and Development Report
JAXA-RR-06-006E